14

Experimental and Theoretical Modelling of 3D Gravity Currents

Michele La Rocca[1] and Allen Bateman Pinzon[2]
Sediment Transport Research Group (GITS-UPC)
[1]University Roma TRE, Dep. of Civil Engineering Sciences, Rome,
[2]Politechnical University of Catalunya, Dep. of Hydraulic, Maritime and Environmental Eng., Barcelona,
[1]Italy
[2]Spain

1. Introduction

When two liquid bodies with different density come in contact in non-equilibrium conditions, a flow is caused, known as gravity or density current. In the environment, as well as in the industrial framework, this kind of flow is very common and the scientific-technical interest of the investigation on it is very high. The paper of Huppert (2006) and the book of Ungarish (2009b) give excellent reviews on the state of the art of the topic, while a huge collection of artificial, as well as natural, gravity currents and a qualitative description of their key features is given in the book of Simpson (1997).
The investigation on gravity currents dates back to several decades ago (first important works are those of Von Karman, 1940; Yih, 1947; Prandtl, 1952 and Keulegan, 1957), nevertheless many aspects still need a better understanding. These aspects should be investigated in order to widen the knowledge on the considered phenomenon and are generally related to the geometry of the fluid domain and the use of particular fluids, like e.g. mixtures of liquid and sediments.
Early studies on gravity currents were based on analytical and experimental methods and were concerned with 2D gravity currents: i.e. gravity currents whose description can be made in a vertical x-z plane. The seminal work of Benjamin (1968) formulates a fundamental theory, based on the perfect-fluid hypothesis and simple extensions of it (like the classical theory of hydraulic jumps), which gives a relationship between the thickness of the gravity current and the velocity of the front. The Benjamin's theory is a milestone and analytical investigations on gravity currents, even the most recent (Shin et al., 2004; Lowe et al., 2005; Ungarish & Zemach, 2005; Ungarish, 2008; Ungarish, 2009) cannot disregard it.
Laboratory gravity currents can be realized in very different ways (Simpson, 1997), depending on which features have to be investigated. The basic experimental setup, which permits to investigate the propagation's features of the gravity current, is the lock exchange release experiment. This experiment consists in leaving two liquid bodies of different density in non-equilibrium condition, typically removing a sliding gate which originally separated them. The consequence is a flow of heavier liquid (the gravity current) under the

lighter liquid. The advancing velocity of the gravity current's front, its thickness and the relation between them are the major issues. The work of Huppert & Simpson (1980) is one of the first works which gives an empirical relation between the velocity and the thickness of the gravity current's front. The validity of the empirical relation of Huppert and Simpson is confirmed by the fact that many experimental results, also of earlier experimental works (Simpson & Britter, 1979), agree well with it. Other experimental studies, as the work of Rottmann & Simpson (1983), highlight also the different phases of the gravity current's evolution (slumping phase, self-similar phase, viscous phase). More complex geometries and fluids are accounted for in recent experimental studies: it is the case of axisymmetric gravity currents (i.e. gravity currents whose description can be made in a radial-vertical *r-z* plane), in fixed and rotating frames, (Hallworth et al., 2001; Hallworth et al., 2003; Patterson et al., 2006; and Ungarish, 2007a) and the case of gravity currents realized with mixtures of water and sediments or with solutions of particular substances and water, which realize a high density difference (Bonnecaze et al., 1993; Lowe et al., 2005). In comparison with 2D and axisymmetric gravity currents, the case of fully 3D gravity currents, whose spatial description needs all of the three spatial coordinates, has been investigated more rarely in the scientific literature. The works of Ross (2002) and La Rocca et al. (2008) are interesting examples

With the increasing development of computational resources, numerical investigations on gravity currents have developed to a considerable extent. There are two main approaches on which numerical investigations are based. The first is represented by the vertically averaged equations of motion (shallow water equations). This approach is justified by the fact that the longitudinal extension of the gravity current has (except for the very initial phase of motion) an order of magnitude L larger than its thickness h. The shallow water approach gives a "technical" description of the gravity current, based on the thickness and the vertically averaged horizontal velocity of this latter, while the fine details of motion are ignored. The first interesting work is that of Rottman & Simpson (1983), focused on 2D gravity currents. Since then, this approach has been giving interesting results, as the works of Bonnecaze et al. (1993), Klemp et al. (1994), D'alessio et al. (1996), Ungarish & Zemach (2005) and Ungarish (2007a) show. The approach based on the vertically averaged equations has been successfully applied to gravity current realized in axisymmetric domains (Hallworth et al., 2003; Ungarish, 2007b; Ungarish, 2010) and to fully 3D gravity currents (La Rocca et al., 2008). Despite of its limitations, the shallow water approach gives reliable insights and fairly accurate predictions (sometimes even better than those obtained by full Navier-Stokes simulations) except for a very short initial phase (Ungarish, 2007b). Additionally, the shallow water solutions reveal features that appear relevant to the more complex two-dimensional simulations (Klemp et al., 1994).

The second numerical approach is based on the complete equations of motion and gives a detailed description of the gravity current motion. It is a recent approach, due to the large computational resources needed, but it has already achieved a considerable development. Some interesting works are those of Härtel et al. (2000a) and Härtel et al. (2000b), who computed a high-resolution direct numerical simulation (DNS) of the flow at the gravity current's head; Birman et al. (2005), who made a DNS of 2D non-Boussinesque gravity currents (i.e., occurring in fluids with large density differences). Hallworth et al. (2001) solved the Navier Stokes equations in a rotating axisymmetric domain. Patterson et al. (2006) characterized the flow structure of the head of an axisymmetric gravity current

evolving in a circular sector of about 10°, and was able to distinguish different stages of the gravity current evolution.

This brief analysis of the recent literature highlights that the attention dedicated to the investigation on fully 3D gravity currents, with constant or variable density, has not had the same extent than that dedicated on 2D and axisymmetric gravity currents.

This chapter is then aimed to give a contribution for the widening of the knowledge on gravity currents, presenting some recent numerical and experimental results obtained on fully 3D gravity currents, with constant and variable density. The structure of the chapter is as follows. After a brief qualitative description of the phenomenon, different mathematical models, corresponding to the case of constant and variable density, are formulated. Then, the main numerical method is explained and the experimental setup is described. At last, after the validation of the mathematical models and the numerical method, experimental and numerical results, obtained for 3D gravity currents with constant and variable density, are presented.

2. Description of the phenomenon

Gravity currents are characterised by a very complex dynamics and a variety of phenomena (Simpson, 1997), represented schematically in Fig. 1.

The gravity current shown in Fig. 1 is generated on an erodible bed after that the two liquid bodies with different densities ρ_1, ρ_2 ($\rho_1>\rho_2$) are put in contact in non equilibrium condition. After some time, the gravity current assumes the characteristic tapered form shown in Fig. 1: the front advances with velocity u_f and has a conventional thickness h_f. The drawing shown in Fig. 1 is not arbitrary and can be compared with the experimental gravity current shown in Fig. 4, realised by means of a lock exchange release experiment at the hydraulic lab of the DEHMA of the Politechnical University of Catalunya, in a transparent channel (length L=2 m, width b=0.2 m, height H=0.35 m), with salty (ρ_1=1100 kgm^{-3}) and fresh water (ρ_2=1000 kgm^{-3}), on a fixed bed. The initial height of the lock was h_1=0.28 m.

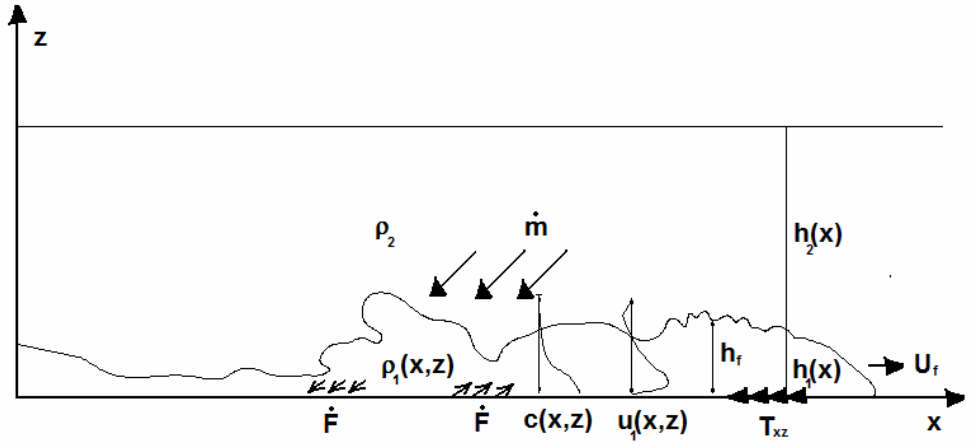

Fig. 1. Sketch of the gravity current

The gravity current represented in Fig.1 flows under a layer of lighter liquid (density ρ_2), whose thickness h_2 is larger than that of the gravity current h_1: quite a common situation. The surface between the gravity current and the liquid layer, represented by a continuous line in Fig. 1, is, in fact, a conventional surface. Increasing z, there is actually a gradual change, although rather abrupt for $z \sim h_1$, of all the quantities characterizing the gravity current.

The gravity current can exchange mass with the lighter liquid by entraining a mass per unit time $\dot{m}$ of lighter liquid. This entrainment of liquid dilutes the density ρ_1, while causing an increase of the gravity current's volume. An exchange of mass, represented by the term $\dot{F}$, can occur also with the bottom, if the gravity current consists of a mixture of liquid and sediment with concentration c. This exchange of mass causes a variation of the density ρ_1, by means of a variation of the concentration of sediment c, and consists in the settling down and re-suspension of sediment. The settling down is caused by the sediment's weight, while the re-suspension is caused by the drag stress exerted by the current on the bottom. This latter, on the other hand, acts on the gravity current by means of a friction stress T_{xz}, which depends on the roughness of the bottom.

All of the quantities which characterize the gravity current depend on the spatial coordinates and time. In particular, in Fig. 1 are shown the profiles of the concentration and the gravity current's velocity c and u_1. Fig. 1 can give an idea of the complexity of the phenomena involved in the gravity current dynamics.

Fig.1 and Fig.4 refer to a 2D gravity current. In Figures 2, 3, the more complex structure of the dynamics of a 3D gravity current can be appreciated. In Figg. 2, 3 are shown the top and side view of the 3D gravity current respectively.

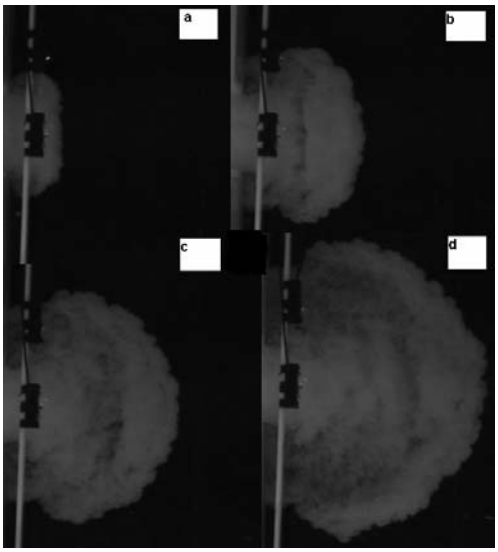

Fig. 2. Top view of a 3D gravity current. a) 2 s; b) 4 s; c) 6 s; d) 8 s after the complete removal of the lock

The gravity currents shown in Figures 2 and 3 were realized by means of a lock exchange release experiment performed at the hydraulic lab of the Dep. of Civil Eng. Sciences of the

University Roma TRE. A transparent rectangular tank, made of two equal square tanks (side L=1 m), was used. A wall, with an opening with width b=0.2 m and closed by a sliding lock, divided the two square tanks. The case shown in Fig. 2 was realized with salty (ρ_1=1015 kgm^{-3}) and fresh water (ρ_2=1000 kgm^{-3}). The initial height of the lock was h_1=0.15 m.

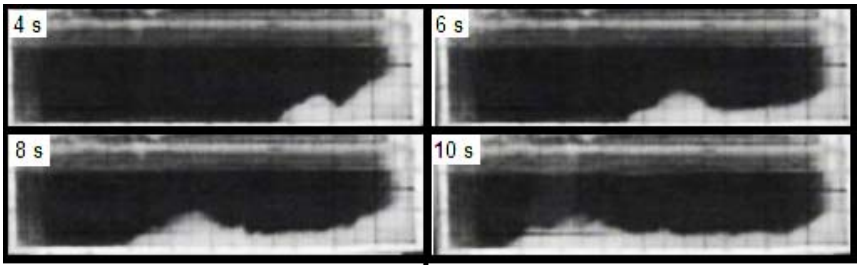

Fig. 3. Side view of a 3D gravity current, 4s, 6s, 8s, 10s after the complete removal of the lock

The case shown in Fig. 3 was realized with salty (ρ_1=1018 kgm^{-3}) and fresh water (ρ_2=1000 kgm^{-3}). The initial height of the lock was h_1=0.20 m.

3. Mathematical models

3.1 Derivation of the shallow water equations for two superimposed liquid layers

Consider two layers of liquids (Fig. 1), whose densities and thicknesses are respectively ρ_1, ρ_2 ($\rho_1>\rho_2$), h_1, h_2. As shown in Fig. 1, the lighter layer is superimposed on the heavier layer and hereinafter reference will be made to the upper or lighter layer and to the lower or heavier layer indifferently.

The densities of the layers will be able to vary slightly, due to the possible mixing between the layers, which occurs across the separation surface between them, and to the sedimentation and re-suspension phenomena. Standard scaling arguments (Pedloski, 1987) and formal perturbative expansions (Stoker, 1957) show that, if the ratio $\delta=h/L$ (being h, L a vertical and a horizontal spatial scale respectively) is such that: $\delta<<1$, the vertical component of the momentum balance equation of the i^{th} layer (i=1,2) is reduced to:

$$\frac{\partial p_i}{\partial z} = -\rho_i g \tag{1}$$

from which, assuming that the density ρ_i does not depend on the vertical coordinate z, the following hydrostatic pressure distributions can be obtained in each layer:

$$p_{\mathbf{2}} = P_s + \rho_{\mathbf{2}} g\left(h_{\mathbf{1}} + h_{\mathbf{2}} + z_f - z\right), \quad p_{\mathbf{1}} = P_s + \rho_{\mathbf{2}} g h_{\mathbf{2}} + \rho_{\mathbf{1}} g\left(h_{\mathbf{1}} + z_f - z\right) \tag{2}$$

The pressure P_s is a reference pressure, defined on the upper surface. If this latter is a free-surface, P_s vanishes. The pressure distributions (2) are a reliable approximation of the actual pressure distribution, at least to order $O(\delta^2)$ (D'Alessio et al., 1996).

Consider the mass balance equation in each layer and integrate it with respect to the vertical coordinate z. Making use of the Leibniz rule and of suitable conditions on the separation surface and on the bottom (D'Alessio, 1996), the following result is obtained:

$$\begin{cases} \dfrac{\partial \rho_1 h_1}{\partial t} + \dfrac{\partial (\rho_1 U_1 h_1)}{\partial x} + \dfrac{\partial (\rho_1 V_1 h_1)}{\partial y} = \dot{m} \\ \dfrac{\partial \rho_1 h_2}{\partial t} + \dfrac{\partial (\rho_1 U_2 h_2)}{\partial x} + \dfrac{\partial (\rho_1 V_2 h_2)}{\partial y} = -\dot{m} \end{cases} \tag{3}$$

All of the quantities appearing in equations (3) are vertically averaged quantities, defined as:

$$\cdot \begin{cases} \displaystyle\int_{z_f}^{h_1+z_f} \rho_1 dz = \rho_1 h_1, \quad \int_{z_f}^{h_1+z_f} \rho_1 u_1 dz = \rho_1 U_1 h_1, \quad \int_{z_f}^{h_1+z_f} \rho_1 v_1 dz = \rho_1 V_1 h_1 \\ \displaystyle\int_{h_1+z_f}^{h_1+h_2+z_f} \rho_2 dz = \rho_2 h_2, \quad \int_{h_1+z_f}^{h_1+h_2+z_f} \rho_2 u_2 dz = \rho_2 U_2 h_2, \quad \int_{h_1+z_f}^{h_1+h_2+z_f} \rho_2 v_2 dz = \rho_2 V_2 h_2 \end{cases} . \tag{4}$$

where z_f is the bottom elevation. In this framework z_f is assumed as a known function of the spatial coordinates and does not depend on time. The bottom profile is given by: z_f=0, if the bottom is flat.

The mass flux between the two liquid layers is accounted for by means of the source term $\dot{m}$ at RHS of equations (3). It is worth observing that the source term appears with positive sign in the mass equation of the first layer and with negative sign in the mass equation of the second layer, then showing consistently that the mass lost by a layer is gained by the other layer and preserving the mass conservation for the fluid system as a whole.

Consider the horizontal components of the momentum equation in each layer and integrate them with respect to the vertical coordinate z, accounting for the hydrostatic pressure distribution (2). Making use of the Leibniz rule and of the abovementioned conditions on the separation surface and on the bottom, the following result is obtained:

$$\begin{cases} \dfrac{\partial \rho_1 U_1 h_1}{\partial t} + \dfrac{\partial}{\partial x}\left(\left(\rho_1 U_1^2 + P_s + \rho_2 g h_2 + \rho_1 g \dfrac{h_1}{2}\right) h_1\right) + \dfrac{\partial \rho_1 U_1 V_1 h_1}{\partial y} = \dot{m} u_{s1} + S_{xss} - S_{xb} - \dfrac{\partial T_{xx}^1}{\partial x} - \dfrac{\partial T_{xy}^1}{\partial y} - \tau_{xss} + \tau_{xb} \\ \dfrac{\partial \rho_1 V_1 h_1}{\partial t} + \dfrac{\partial \rho_1 U_1 V_1 h_1}{\partial x} + \dfrac{\partial}{\partial y}\left(\left(\rho_1 V_1^2 + P_s + \rho_2 g h_2 + \rho_1 g \dfrac{h_1}{2}\right) h_1\right) = \dot{m} v_{s1} + S_{yss} - S_{yb} - \dfrac{\partial T_{yx}^1}{\partial x} - \dfrac{\partial T_{yy}^1}{\partial y} - \tau_{yss} + \tau_{yb} \\ \dfrac{\partial \rho_2 U_2 h_2}{\partial t} + \dfrac{\partial}{\partial x}\left(\left(\rho_2 U_2^2 + P_s + \rho_2 g \dfrac{h_2}{2}\right) h_2\right) + \dfrac{\partial \rho_2 U_2 V_2 h_2}{\partial y} = -\dot{m} u_{s2} + S_{xus} - S_{xss} - \dfrac{\partial T_{xx}^2}{\partial x} - \dfrac{\partial T_{xy}^2}{\partial y} - \tau_{xus} + \tau_{xss} \\ \dfrac{\partial \rho_2 V_2 h_2}{\partial t} + \dfrac{\partial \rho_2 U_2 V_2 h_2}{\partial x} + \dfrac{\partial}{\partial y}\left(\left(\rho_2 V_2^2 + P_s + \rho_2 g \dfrac{h_2}{2}\right) h_2\right) = -\dot{m} v_{s2} + S_{yus} - S_{yss} - \dfrac{\partial T_{yx}^2}{\partial x} - \dfrac{\partial T_{yy}^2}{\partial y} - \tau_{yus} + \tau_{ys} \end{cases} \tag{5}$$

The momentum fluxes exchanged by the liquid layers due to the mass flux $\dot{m}$ are accounted for by means of the horizontal components of the liquid velocity on the separation surface: $u_{s1}, v_{s1}, u_{s2}, v_{s2}$. The quantities S_{xss}, S_{xb}, S_{xus} and S_{yss}, S_{yb}, S_{yus} are the horizontal components of the pressure forces on the separation surface (*ss*), the bottom (*b*) and the upper surface (*us*). They are defined as:

$$\begin{cases} S_{xss} = \left(P_s + \rho_{\mathbf{2}} g h_{\mathbf{2}}\right)\dfrac{\partial}{\partial x}\left(h_{\mathbf{1}} + z_f\right), S_{xb} = \left(P_s + \rho_{\mathbf{2}} g h_{\mathbf{2}} + \rho_{\mathbf{1}} g h_{\mathbf{1}}\right)\dfrac{\partial z_f}{\partial x}, S_{xus} = P_s \dfrac{\partial}{\partial x}\left(h_{\mathbf{1}} + h_{\mathbf{2}} + z_f\right) \\ S_{yss} = \left(P_s + \rho_{\mathbf{2}} g h_{\mathbf{2}}\right)\dfrac{\partial}{\partial y}\left(h_{\mathbf{1}} + z_f\right), S_{yb} = \left(P_s + \rho_{\mathbf{2}} g h_{\mathbf{2}} + \rho_{\mathbf{1}} g h_{\mathbf{1}}\right)\dfrac{\partial z_f}{\partial y}, S_{yus} = P_s \dfrac{\partial}{\partial y}\left(h_{\mathbf{1}} + h_{\mathbf{2}} + z_f\right) \end{cases} \quad (6)$$

The quantities $\tau_{ij}^{k}, k = \mathbf{1},\mathbf{2}; i = x, y; j = x, y$ represent the vertically average viscous and turbulent stresses and the dispersive stresses. The quantities $\tau_{xss}, \tau_{xb}, \tau_{xus}$ and $\tau_{yss}, \tau_{yb}, \tau_{yus}$ are the horizontal components of the stress $\boldsymbol{\tau}$ on the separation surface (τ_{xss}, τ_{yss}), the bottom (τ_{xb}, τ_{yb}) and the upper surface (τ_{xus}, τ_{yus}). Equations (3) and (5) are put in the most general form, from which it is possible to derive all of the shallow water approximations concerning the motion of two liquid layers with slightly varying densities.

3.2 The case of two immiscible liquids with constant density

The case of two immiscible liquids with constant densities is representative for gravity currents realized with water and a soluble matter (e.g. NaCl), when the Richardson number

$$Ri = \frac{\rho_{\mathbf{1}} - \rho_{\mathbf{2}}}{\rho_{\mathbf{2}}} \frac{gh}{U^{\mathbf{2}}} \quad (7)$$

has an order of magnitude larger than 1 (Fischer et al., 1979). Indeed, the Richardson number, calculated with the velocity and thickness scales U, h, is the ratio of the order of magnitude of hydrostatic forces to the order of magnitude of inertial forces: if the former dominate, i.e. if Ri>1, mixing between the two liquid layers is hindered by the stratification and can be neglected. The gravity currents realized with water and a soluble matter are known as conservative gravity currents, because the matter dissolved in water is conserved, and are distinguished from those realized with mixtures of water and sediments, whose density can change due to sedimentation and re-suspension processes. Variations of density in conservative gravity currents are possible only due to the entrainment of lighter liquid, which occurs at the separation surface, as shown in Fig. 4, where the red ellipses indicate the part of the gravity current affected by the entrainment of lighter liquid.

As a consequence of the immiscibility hypothesis, the mass flux $\dot{m}$ is zero. Moreover, it is a usual assumption to neglect the stresses $\tau_{ij}^{k}, k = \mathbf{1},\mathbf{2}; i = x, y; j = x, y$ (Ungarish, 2009). This assumption is based on the estimate of the Reynolds number of the current and on the difficulty in modeling dispersive stresses. The Reynolds number of the current is defined by:

$$Re = \frac{h}{\nu}\sqrt{\frac{\rho_1 - \rho_2}{\rho_1} gh} \quad (8)$$

and is usually very high, due to the small value of the kinematic viscosity and the moderate values of the gravity current's height. As an example, the value of the Reynolds number of the gravity current shown in Fig. 4, assuming h=0.1 m, ν=10^{-6} m^2s^{-1}, is equal to: $Re = \mathbf{3} \times \mathbf{10^4}$, showing that the gravity current is in turbulent motion. Only the stresses τ_{xb}, τ_{yb} will be retained. Indeed, they are exerted on the lower layer by the bottom and are surely more important than the stresses acting on the separation surface τ_{xss}, τ_{yss} and the stresses acting on the upper surface τ_{xus}, τ_{yus}. These latter vanish if the upper surface is a free surface.

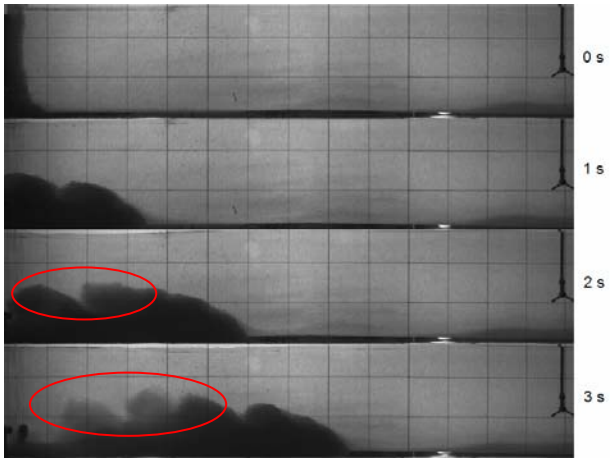

Fig. 4. Experimental profile of a 2D gravity current

$$
\begin{cases}
\dfrac{\partial h_1}{\partial t}+\dfrac{\partial (U_1 h_1)}{\partial x}+\dfrac{\partial (V_1 h_1)}{\partial y}=0 \\
\dfrac{\partial h_2}{\partial t}+\dfrac{\partial (U_2 h_2)}{\partial x}+\dfrac{\partial (V_2 h_2)}{\partial y}=0 \\
\dfrac{\partial U_1 h_1}{\partial t}+\dfrac{\partial}{\partial x}\left(U_1^2 h_1+g\dfrac{h_1^2}{2}\right)+\dfrac{\partial U_1 V_1 h_1}{\partial y}+\dfrac{\rho_2}{\rho_1}gh_1\dfrac{\partial h_2}{\partial x}=-\dfrac{h_1}{\rho_1}\dfrac{\partial P_s}{\partial x}-gh_1\dfrac{\partial z_f}{\partial x}+\dfrac{\tau_{xb}}{\rho_1} \\
\dfrac{\partial V_1 h_1}{\partial t}+\dfrac{\partial U_1 V_1 h_1}{\partial x}+\dfrac{\partial}{\partial y}\left(V_1^2 h_1+g\dfrac{h_1^2}{2}\right)+\dfrac{\rho_2}{\rho_1}gh_1\dfrac{\partial h_2}{\partial y}=-\dfrac{h_1}{\rho_1}\dfrac{\partial P_s}{\partial y}-gh_1\dfrac{\partial z_f}{\partial y}+\dfrac{\tau_{yb}}{\rho_1} \\
\dfrac{\partial U_2 h_2}{\partial t}+\dfrac{\partial}{\partial x}\left(U_2^2 h_2+g\dfrac{h_2^2}{2}\right)+\dfrac{\partial U_2 V_2 h_2}{\partial y}+gh_2\dfrac{\partial h_1}{\partial x}=-\dfrac{h_2}{\rho_2}\dfrac{\partial P_s}{\partial x}-gh_2\dfrac{\partial z_f}{\partial x} \\
\dfrac{\partial V_2 h_2}{\partial t}+\dfrac{\partial U_2 V_2 h_2}{\partial x}+\dfrac{\partial}{\partial y}\left(V_2^2 h_2+g\dfrac{h_2^2}{2}\right)+gh_2\dfrac{\partial h_1}{\partial y}=-\dfrac{h_2}{\rho_2}\dfrac{\partial P_s}{\partial y}-gh_2\dfrac{\partial z_f}{\partial y}
\end{cases}
\tag{9}
$$

At last, also the velocities $u_{s1}, v_{s1}, u_{s2}, v_{s2}$ are neglected. With these hypothesis equations (3) and (5) reduce to the equations (9). These equations, together with proper initial and boundary conditions, represent a very difficult problem for numerical integration. Even when the upper surface is a free surface and then the pressure P_s vanishes on it, the equations (9) form a partial differential system of six equations in non conservative form, fact which makes difficult the application of numerical methods with good shock-capturing and shock-fitting features (La Rocca et al., 2008). Moreover, performing the analysis of the eigenvalues of the partial differential system (9), it is found that wide ranges of the relevant physical parameters exist where these eigenvalues are complex, then revealing the non-hyperbolicity nature of the partial differential system (9). The loss of hyperbolicity causes instability during numerical integration (Garabedian, 1964; Bradford et al., 1997; Lyczkowski et al., 1978; Lee & Lyczkowski, 2000).

In order to overcome the abovementioned difficulties, assume the rigid-lid hypothesis, according to which the sum of the liquid layers thicknesses is constant with respect time and space:

$$h_1 + h_2 + z_f = H \tag{10}$$

being H the initial elevation of the upper surface. The consequences of the rigid-lid hypothesis are very interesting. Firstly, the mass balance equation for the upper layer is substituted by the algebraic relation (10) and the partial differential system (9) becomes:

$$\begin{cases} \dfrac{\partial h_1}{\partial t} + \dfrac{\partial (U_1 h_1)}{\partial x} + \dfrac{\partial (V_1 h_1)}{\partial y} = 0 \\ \dfrac{\partial U_1 h_1}{\partial t} + \dfrac{\partial}{\partial x}\left(U_1^2 h_1 + g\left(1 - \dfrac{\rho_2}{\rho_1}\right)\dfrac{h_1^2}{2}\right) + \dfrac{\partial U_1 V_1 h_1}{\partial y} = -\dfrac{h_1}{\rho_1}\dfrac{\partial P_s}{\partial x} - g\left(1 - \dfrac{\rho_2}{\rho_1}\right) h_1 \dfrac{\partial z_f}{\partial x} + \dfrac{\tau_{xb}}{\rho_1} \\ \dfrac{\partial V_1 h_1}{\partial t} + \dfrac{\partial U_1 V_1 h_1}{\partial x} + \dfrac{\partial}{\partial y}\left(V_1^2 h_1 + g\left(1 - \dfrac{\rho_2}{\rho_1}\right)\dfrac{h_1^2}{2}\right) = -\dfrac{h_1}{\rho_1}\dfrac{\partial P_s}{\partial y} - g\left(1 - \dfrac{\rho_2}{\rho_1}\right) h_1 \dfrac{\partial z_f}{\partial y} + \dfrac{\tau_{yb}}{\rho_1} \\ \dfrac{\partial U_2 h_2}{\partial t} + \dfrac{\partial}{\partial x}\left(U_2^2 h_2\right) + \dfrac{\partial U_2 V_2 h_2}{\partial y} = -\dfrac{h_2}{\rho_2}\dfrac{\partial P_s}{\partial x} \\ \dfrac{\partial V_2 h_2}{\partial t} + \dfrac{\partial U_2 V_2 h_2}{\partial x} + \dfrac{\partial}{\partial y}\left(V_2^2 h_2\right) = -\dfrac{h_2}{\rho_2}\dfrac{\partial P_s}{\partial y} \end{cases} \tag{11}$$

Secondly, the pressure P_s does not vanish, as the upper surface is no more a free surface, being forced to remain flat. The pressure P_s represents the actual coupling term between the two liquid layers. Indeed, fourth and fifth equations (11) do not contain any forcing term, but the pressure terms. If these happen to vanish, the two liquid layers are uncoupled and the evolution of the lower layer cannot influence that of the upper layer.

Thirdly, the presence of the pressure P_s represents a non trivial problem in solving the equations (11). Indeed, while in the 2D and axisymmetric cases the pressure P_s can be easily eliminated from the motion equations (Rottmann & Simpson, 1983; Ungarish & Zemach, 2005), for the general case presented here this is not possible. The pressure P_s must be determined solving the motion equations together with a specific equation, which can be obtained starting from the following observation: the vector field $\boldsymbol{\upsilon}$ ($\boldsymbol{\upsilon} \equiv \{U_1 h_1 + U_2 h_2, V_1 h_1 + V_2 h_2\}$) is divergence free. Indeed, add the mass balance equations of the two liquid layers and account for (10):

$$\frac{\partial (h_1 + h_2)}{\partial t} + \frac{\partial (U_1 h_1 + U_2 h_2)}{\partial x} + \frac{\partial (V_1 h_1 + V_2 h_2)}{\partial y} = 0 \quad \Rightarrow \quad \frac{\partial (U_1 h_1 + U_2 h_2)}{\partial x} + \frac{\partial (V_1 h_1 + V_2 h_2)}{\partial y} = 0 \tag{12}$$

Then sum second and fourth equation (11) and third and fifth equation (11), differentiate these sums with respect to x and y, sum them again and account for the divergence free condition (12): as a consequence the following Poisson equation is obtained for the pressure P_s:

$$\frac{\partial}{\partial x}\left(\left(\frac{h_1}{\rho_1}+\frac{h_2}{\rho_2}\right)\frac{\partial P_s}{\partial x}\right)+\frac{\partial}{\partial y}\left(\left(\frac{h_1}{\rho_1}+\frac{h_2}{\rho_2}\right)\frac{\partial P_s}{\partial y}\right)=-\frac{\partial^2}{\partial x^2}\left(U_1^2h_1+U_2^2h_2+g'\frac{h_1^2}{2}\right)-2\frac{\partial^2}{\partial y\partial x}\left(U_1V_1h_1+U_2V_2h_2\right)$$
$$-\frac{\partial^2}{\partial y^2}\left(V_1^2h_1+V_2^2h_2+g'\frac{h_1^2}{2}\right)-\frac{\partial}{\partial x}\left(g'h_1\frac{\partial z_f}{\partial x}-\frac{\tau_{xb}}{\rho_1}\right)-\frac{\partial}{\partial y}\left(g'h_1\frac{\partial z_f}{\partial y}+\frac{\tau_{yb}}{\rho_1}\right) \quad (13)$$

being the reduced gravity g' defined as: $g'=g\left(1-\rho_2/\rho_1\right)$.

So, in the framework of the shallow water formulation, the dynamics of two layers of immiscible liquids, with a rigid lid, is governed by the equations (11), (13), given suitable initial and boundary conditions. Initial conditions refer generally to motions starting from a quiescent configuration with a given shape of the lower layer thickness:

$$U_1(x,y,0)=0, V_1(x,y,0)=0, U_2(x,y,0)=0, V_2(x,y,0)=0, h_1(x,y,0)=f(x,y) \quad (14)$$

Boundary conditions are imposed in correspondence of rigid, impermeable surfaces. The normal velocity component and the normal derivative of the pressure vanish on these surfaces:

$$U_1n_x+V_1n_y=0,\ U_2n_x+V_2n_y=0,\ \frac{\partial P_s}{\partial x}n_x+\frac{\partial P_s}{\partial y}n_y=0 \quad (15)$$

The first two boundary conditions (15) are physically consistent, while the third satisfies the solvability condition obtained integrating the Poisson equation (13) on the fluid domain.
The equations (11), (13), with the initial and boundary conditions (14), (15), set up the rigid-lid, two-layer formulation for 3D gravity currents with constant density.

3.3 The case of two liquid layers with variable density

In this case the density of the heavier layer can change mainly as a consequence of a sedimentation-resuspension dynamics. This case is representative for subaqueous turbidity currents, occurring e.g. when a heavy current of water and sediments flows under a lake or a sea. In this framework, variations of density due to temperature are considered of minor importance, although they can be accounted for by means of a suitable thermal energy balance (Pratson et al., 2001), which however will not be considered for the sake of simplicity. These turbidity currents form at the bottom of great water basins and represent an important mechanism of transport of sediments in deep water (Parker et al., 1986). Turbidity currents can attain high velocities (8-14 m/s) (Huang et al. 2005), they can be characterized by time scales varying from hours to weeks and flow inside of submarine canyons, which can attain depths of hundreds of meters, widths of thousands of meters and lengths of thousands of kilometers (Birman et al., 2009). These currents can damage the submarine structures (pipes, cables) they interact with and can change the morphology of the bottom, due to erosion and sedimentation (Kostic & Parker, 2007; Cantero et al., 2008). Moreover, turbidity currents can affect the quality of water, depending on the sediments they are made of. This is an environmental problem of increasing importance and it is worth examining briefly the case study of the artificial reservoir of Flix, situated near Tarragona, Spain (Costa et al. 2004). This artificial water reservoir, built on the river Ebro in 1948 for irrigation, water storage and production of energy, caused the accumulation of contaminated sediments, resulting from the chemical processes of a factory situated 700 meters upstream of the reservoir in the right margin of the Ebro. The contaminated

sediments, accumulated during over fifty years of industrial activity, contained very dangerous substances as DDT, Hexachlorineethylene, PCB, bicalcic phosphate, Mercury, Cyanide. On December 22nd 2001, after several days of very low temperatures, thousands of dead fish appeared in the river Ebro, close to the Flix reservoir, and the water analysis, carried out at the entrance of supply water plants of important cities as Tarragona, revealed levels of concentration of Mercury much higher than the normal. The most probable explanation of this fact was that the particular meteorological conditions could have caused a current of cold and dense water with enough strength to entrain the sediment from the bed and, therefore, to mix mercury with water. The resulting concentration of Mercury caused the murrain of fishes and made unusable the water for several months.

The mathematical modeling of this kind of gravity current, known as turbidity current, is very complicate. Here the approach of Pratson et al. (2001) will be followed and extended to the general 3D case. It is assumed that (Pratson et al., 2001; Kostic and Parker, 2007) the heavier liquid is a mixture made with a uniform sediment, characterized by a median diameter d_s, with depth averaged concentration C, flowing under an infinite layer of water. This latter assumption is very important, because it is possible to show that, as a consequence of it (Ungarish & Zemach, 2005; La Rocca & Bateman, 2010), the pressure P_s vanishes and the motion of the upper layer becomes negligible. Then the well known one layer formulation is obtained for the turbidity current and a considerable reduction of the equations number follows, because only the mass and momentum balance equations of the turbidity current have to be considered. Having introduced the depth averaged concentration C, the density of the heavy liquid layer is given by:

$$\rho_{\mathbf{1}} = \rho_{\mathbf{2}}(1-C) + \rho_s C = \rho_{\mathbf{2}} + (\rho_s - \rho_{\mathbf{2}})C \tag{16}$$

being ρ_s the density of the sediments. In dealing with such gravity currents, it is usual to assume that the ratio:

$$\frac{\rho_{\mathbf{1}} - \rho_{\mathbf{2}}}{\rho_{\mathbf{2}}} = \frac{\rho_s - \rho_{\mathbf{2}}}{\rho_{\mathbf{2}}} C = RC \tag{17}$$

is small. R is defined as: $R = (\rho_s - \rho_{\mathbf{2}})/\rho_{\mathbf{2}}$. The consequence is that the Boussinesq's approximation is valid (Kostic & Parker, 2007), according to which the changes in the density ρ_1 are considered important only in the gravitational term. Substituting definition (16) in the partial differential system (5) and accounting for the Boussinesq's approximation, the mass and momentum balance equations assume the following form:

$$\begin{cases} \dfrac{\partial h_{\mathbf{1}}}{\partial t} + \dfrac{\partial U_{\mathbf{1}} h_{\mathbf{1}}}{\partial x} + \dfrac{\partial V_{\mathbf{1}} h_{\mathbf{1}}}{\partial y} = \dot{q} \\ \dfrac{\partial U_{\mathbf{1}} h_{\mathbf{1}}}{\partial t} + \dfrac{\partial U_{\mathbf{1}}^{\mathbf{2}} h_{\mathbf{1}}}{\partial x} + \dfrac{\partial U_{\mathbf{1}} V_{\mathbf{1}} h_{\mathbf{1}}}{\partial y} + Rg \dfrac{\partial}{\partial x}\left(C h_{\mathbf{1}}^{\mathbf{2}}/\mathbf{2}\right) = \dot{q} u_s + \tau_{xb} - g h_{\mathbf{1}} \dfrac{\partial z_f}{\partial x} \\ \dfrac{\partial V_{\mathbf{1}} h_{\mathbf{1}}}{\partial t} + \dfrac{\partial U_{\mathbf{1}} V_{\mathbf{1}} h_{\mathbf{1}}}{\partial x} + \dfrac{\partial V_{\mathbf{1}}^{\mathbf{2}} h_{\mathbf{1}}}{\partial y} + Rg \dfrac{\partial}{\partial y}\left(C h_{\mathbf{1}}^{\mathbf{2}}/\mathbf{2}\right) = \dot{q} v_s + \tau_{yb} - g h_{\mathbf{1}} \dfrac{\partial z_f}{\partial y} \end{cases} \tag{18}$$

The mass exchange between the two layers is accounted for by means of the quantity $\dot{q}$: it represents the volume of water per unit surface and time, entrained by the heavier layer,

and is related to the mass per unit surface and time $\dot{m}$ exchanged between the two layers by the approximate relations: $\dot{q} \approx \dot{m}/\rho_{\mathbf{1}} \approx \dot{m}/\rho_{\mathbf{2}}$. The approximation is valid if RC<<1.
Due to the presence of the concentration C as a new variable, another equation is needed. Such an equation is obtained vertically averaging the sediment mass balance equation within the heavier layer. Omitting the details, the following equation is obtained:

$$\frac{\partial C h_{\mathbf{1}}}{\partial t} + \frac{\partial C U_{\mathbf{1}} h_{\mathbf{1}}}{\partial x} + \frac{\partial C V_{\mathbf{1}} h_{\mathbf{1}}}{\partial x} = c_{ss}\dot{q} + \frac{\partial}{\partial x}\left(K_x h_{\mathbf{1}} \frac{\partial C}{\partial x} \right) + \frac{\partial}{\partial y}\left(K_y h_{\mathbf{1}} \frac{\partial C}{\partial y} \right) + \dot{F} \tag{19}$$

where K_x, K_y are the dispersion coefficients along x and y directions (Fischer, 1979) and c_{ss} is the concentration of sediment at the separation surface. The term $\dot{F}$ represents the flux of mass at the bottom and accounts for the sedimentation and re-suspension phenomena.
Initial and boundary conditions have to be imposed on the gravity current's thickness, on the velocity components and on the average concentration. Initial and boundary conditions on the gravity current's thickness and on the velocity components are identical to conditions (14) and (15). With regard to averaged concentration C, a given shape of the initial concentration is imposed as initial condition, while a vanishing mass flux is used as boundary condition, in correspondence of impermeable and fixed boundaries:

$$\begin{cases} U_{\mathbf{1}}(x,y,\mathbf{0}) = \mathbf{0}, V_{\mathbf{1}}(x,y,\mathbf{0}) = \mathbf{0}, h_{\mathbf{1}}(x,y,\mathbf{0}) = f(x,y), \quad U_{\mathbf{1}} n_x + V_{\mathbf{1}} n_y = \mathbf{0} \\ C(x,y,\mathbf{0}) = f_C(x,y), \quad K_x \dfrac{\partial C}{\partial x} n_x + K_y \dfrac{\partial C}{\partial y} n_y - C\left(U_{\mathbf{1}} n_x + V_{\mathbf{1}} n_y\right) = \mathbf{0} \end{cases} \tag{20}$$

3.4 Closure relations

The proposed mathematical models (eqs. (11), (13) and eqs. (18), (19)) contain the unknown terms: $\dot{q}, \tau_{xb}, \tau_{yb}, u_s, v_s, c_{ss}, \dot{F}, K_x, K_y$ whose meaning has been previously introduced. However, the simulation of realistic cases needs the definition of these unknown terms as functions of the resolved variables. In other words, it is necessary to introduce proper closure relations.
The volume flux of entrained liquid $\dot{q}$ per unit surface has the physical dimensions of a velocity. For this reason is expressed as the product of the dimensionless entrainment coefficient e_w by the entrainment velocity U_e :

$$\dot{q} = e_w U_e \tag{21}$$

Following Kostic & Parker (2007), the entrainment coefficient e_w can be estimated by means of:

$$e_w = \frac{\mathbf{0.00153}}{\mathbf{0.0204} + Ri} \tag{22}$$

Being Ri the Richardson number (7). The entrainment velocity can be estimated by the modulus of the velocity of the heavier layer:

$$U_e = \sqrt{U_{\mathbf{1}}^{\mathbf{2}} + V_{\mathbf{1}}^{\mathbf{2}}} \tag{23}$$

The terms τ_{xb}, τ_{yb} are the tangential stresses exerted on the heavier layer by the bottom. In the case of constant densities they can be expressed by means of a friction coefficient λ:

$$\tau_{xb} = \rho_1 \lambda U_1 \sqrt{U_1^2 + V_1^2}, \quad \tau_{yb} = \rho_1 \lambda V_1 \sqrt{U_1^2 + V_1^2} \tag{24}$$

The friction coefficient can be in turn expressed by means of empirical formulas which make use of the gravity current Reynolds number (8) and the roughness of the bottom (see e.g. Cengel & Cimbala, 2006). In the case of variable density the terms τ_{xb}, τ_{yb} are usually expressed by means of the friction velocity, which in turn is assumed proportional to the vertically averaged turbulent kinetic energy K (Parker, 1986):

$$\begin{cases} \tau_{xb} = \rho_2 \dfrac{U_1}{\sqrt{U_1^2 + V_1^2}} u_*^2 \quad \tau_{yb} = \rho_2 \dfrac{V_1}{\sqrt{U_1^2 + V_1^2}} u_*^2 \\ u_*^2 = \alpha K \end{cases} \tag{25}$$

The proportionality constant α is usually given the value 0.1 (Pratson et al., 2001), while the vertically averaged turbulent kinetic energy K is determined by the empirical equation:

$$\frac{\partial K}{\partial t} + U_1 \frac{\partial K}{\partial x} + V_1 \frac{\partial K}{\partial y} = \frac{u_*^2 \sqrt{U_1^2 + V_1^2}}{h_1} + \frac{\left(U_1^2 + V_1^2\right)\dot{q}}{2h_1} - \beta \frac{K^{3/2}}{h_1} - Rg\left[C\left(W_s + \frac{\dot{q}}{2}\right) + W_s \dot{\mathcal{F}}\right] - \dot{q}\frac{K}{h_1} \tag{26}$$

The various terms at RHS of (26) represent respectively: the production of kinetic energy due to turbulence, the production of kinetic energy due to the entrained liquid, the viscous dissipation of energy, the kinetic energy spent to hold the sediment in suspension (proportional to the sediment settling velocity W_s), the kinetic energy spent to maintain in turbulent motion the entrained lighter liquid, the kinetic energy lost (if $\dot{\mathcal{F}} < 0$) or gained (if $\dot{\mathcal{F}} > 0$) due to the sedimentation-re-suspension dynamics, the kinetic energy spent to maintain the entrained lighter liquid in turbulent motion. The empirical coefficient β is calculated as in Launder & Spalding (1972).

The velocity components and the concentration on the separation surface (u_s, v_s, c_{ss}) can be neglected. Indeed the velocity within the turbidity current increases from the bottom up to a maximum value and then decreases uniformly, until it attains a negligible value in correspondence of the separation surface, while the concentration on the separation surface decreases uniformly from the bottom, where it attains its maximum value (Fig. 1).

The diffusive flux of mass $\dot{\mathcal{F}}$ occurring in correspondence of the bottom is due to the settling and the re-suspension of sediment. It can be put in the form (Kostic & Parker, 2007):

$$\dot{\mathcal{F}} = W_s\left(E_s - r_0 C\right) \tag{27}$$

where W_s is the sediment settling velocity. This latter can be calculated following Dietrich (1982), as a function of the non dimensional sediment diameter d^* ($d^* = R\frac{g d_s^3}{\nu^2}$).

The non dimensional erosion coefficient E_s accounts for the entrainment of sediment and, according to Parker & Garcia (1993), is expressed as a function of the non dimensional parameter Z ($Z = \frac{u_*}{W_s \nu}\sqrt{Rg d_s^3}$). Anyway, the non dimensional erosion coefficient E_s is often

assumed to be negligible with respect to the concentration of sediment at the bottom (Kostic & Parker, 2007), which is usually assumed proportional to the vertically averaged concentration C, by means of the dimensionless coefficient r_0 ($r_0 \geq 1$).

At last, the dispersion coefficients K_x, K_y can be defined in terms of the friction velocity and the gravity current's thickness, by means of empirical formulas, as e. g. those of Fischer et al. (1979). Such formulas are usually referred to the case of the dispersion of contaminant in a fluvial stream and, when used in a different context, the numerical values of the dispersion coefficients are affected by large uncertainty. Moreover, the turbidity current's dynamics is dominated by inertia and buoyancy forces, whose effects are more important than those due to the dispersion of sediment. Due to these reasons we will set the dispersion coefficients to zero.

4. Numerical methods

A good numerical method, able to deal with the mathematical models developed in the previous section, should be able to reproduce correctly the key features of the considered phenomenon. These key features refer to the propagation of the front and to the sharp variations of the relevant physical quantities occurring in a narrow spatial interval between the gravity current and the lighter liquid. In other words, a good numerical method should possess good shock-fitting and shock-capturing characteristics.

The mathematical models formulated in the previous section refer to two particular cases: the constant density case and the variable density case. In the case of constant density, the mathematical model consists of the motion equations (11), of the Poisson equation (13) and the initial and boundary conditions (14), (15). In the case of variable density, the mathematical model consists of the motion equations (18), the concentration equation (19), the turbulent kinetic energy equation (26) and the initial and boundary conditions (20). Moreover, closure relations are integrant part of both the mathematical models.

The proposed mathematical models are rather complex. The strong coupling existing between the motion equations and the Poisson equation in the constant density case is particularly challenging. Anyway, by means of a suitable scaling and a formal perturbative expansion (La Rocca & Bateman, 2010), it is possible to eliminate this strong coupling and to adopt a solution procedure valid both for the constant and the variable density case. It is worth showing the essential points of the simplification of the motion equations, omitting the details of the scaling and the formal perturbative expansion. Consider equations (11) in the compact form:

$$\frac{\partial \mathbf{U}}{\partial t} + \frac{\partial \mathbf{F}}{\partial x} + \frac{\partial \mathbf{G}}{\partial y} = -\mathbf{P} + \mathbf{S} \tag{28}$$

being $\mathbf{U}$ the vector whose components are the conserved variables: $\mathbf{U} \equiv \{h_1, U_1 h_1, V_1 h_1, U_2 h_2, V_2 h_2\}$. The vectors **F, G, P, S** depend on the vector $\mathbf{U}$ and can be defined comparing equations (11) with the compact form (28). Decompose $\mathbf{U}$ as: $\mathbf{U}=\mathbf{U}_0+\mathbf{U}_c$. $\mathbf{U}_0$ satisfies the partial differential system:

$$\frac{\partial \mathbf{U_0}}{\partial t} + \left(\frac{\partial \mathbf{F}}{\partial x} + \frac{\partial \mathbf{G}}{\partial y} \right)\Bigg|_{\mathbf{U}=\mathbf{U_0}} = \mathbf{S}|_{\mathbf{U}=\mathbf{U_0}} \tag{29}$$

and has the remarkable property that its components $U_2 h_2|_0, V_2 h_2|_0$ are zero. Indeed, the evolution of $U_2 h_2|_0, V_2 h_2|_0$ is described by the last two equations of the partial differential

system (11) without the pressure term. These two equations are homogeneous and so, if the initial values of $U_2 h_2\big|_0, V_2 h_2\big|_0$ are zero, they remain zero. The partial differential system (29) is also known as the one-layer model, because it can be thought as a model which ignores completely the motion of the upper layer. It is possible to derive formally this one-layer model (La Rocca & Bateman, 2010) as the leading order approximation of a perturbative expansion of **U** and the partial differential system (28) with respect to the small parameter h/H, being h the order of magnitude of the gravity current's thickness and H the sum of the thicknesses of the upper layer and the gravity current. The one-layer model is obtained in the limit $h/H \to 0$ ($H \to \infty$) (Ungarish & Zemach, 2005) and can be applied when the gravity current's thickness is expected to be negligible with respect to the thickness of the ambient liquid. Nevertheless, the one-layer model (29) is widely applied in the investigation of 2D, axisymmetric and 3D gravity currents also when the ratio $h/H \to 0$ is not small and results are generally good (Ungarish, 2007a; Ungarish, 2007b; Ungarish, 2010; La Rocca et al., 2008). Once the one-layer solution $\mathbf{U_0}$ is known, it is possible to determine a first approximation of the pressure P_S, solving the Poisson equation (13), with the RHS calculated in correspondence of the one-layer solution $\mathbf{U_0}$. Having determined the pressure P_S, it is possible to determine the correction $\mathbf{U_c}$ by means of:

$$\frac{\partial \mathbf{U}_c}{\partial t} + \frac{\partial}{\partial \mathbf{U}}\left(\frac{\partial \mathbf{F}}{\partial x} + \frac{\partial \mathbf{G}}{\partial y}\right)\Bigg|_{\mathbf{U}=\mathbf{U_0}} \mathbf{U}_c = -\mathbf{P} \tag{30}$$

Solving again the Poisson equation with the RHS calculated in correspondence of $\mathbf{U_0}+\mathbf{U_c}$, a better approximation of P_S is obtained. In turn, a new value of the correction can be determined from equations (30) and so on.

The core of the numerical model consists then in solving the one-layer partial differential system. This latter is fundamental not only in the constant but also in the variable density case, as the partial differential system (18) and the concentration equation (19) have the same structure of the one-layer partial differential system (29). The other steps of both the cases can be dealt with standard numerical methods: e.g. the Poisson equation can be solved with a SOR iterative method, while the partial differential system (30) can be solved with a Lax-Wendroff method.

The one layer partial differential system (29), being in conservative form, can be dealt with a finite volume numerical method, particularly suitable to deal with propagation of sharp discontinuities. The book of Toro (1999) is an excellent guide to these methods and shows that the Godunov formulation together with the use of an approximate Riemann solver is a common choice in dealing with hydraulic problems.

In this chapter the Godunov formulation with the approximate Riemann solver of Roe will be adopted for the solution of the one-layer partial differential system (29). The details of the numerical method and of its application to the present case are however omitted, for the sake of simplicity. The reader can find them in the book of Toro (1999) and in the papers of La Rocca et al. (2008), La Rocca et al. (2009).

5. Experimental setup for the realisation of 3D gravity currents

The setup, realized in the Hydraulics Lab of the University Roma TRE (Fig. 5), is a 3D, full-depth, lock exchange release experiment and it consists of a rectangular tank, divided into

two square parts (side L=1 m) by a rigid wall, filled with tap water (density ρ_2) and salty water (density ρ_1, $\rho_1>\rho_2$) up to the same height H. At the centre of the wall there is a sliding gate AB which can be manually removed. The width of the gate is b=0.2 m. The flat bottom of the tank (z_f=0) can be smooth or be made rough by gluing on it uniform sediments, with diameter ε. A CCD video camera records the evolution of the gravity current with an acquisition frequency of 25 Hz. The images obtained from the records are digitized and analysed, so the instantaneous shape of the gravity current is obtained. In general, the top view of the gravity current is considered. Only in few cases the lateral view of the gravity current has been considered too (Fig. 3), but this latter can be used mainly for qualitative comparisons, being the image strongly distorted.
The preparation of the heavier liquid is very simple. It consists in adding a mass m_s of salt to the water, determined in order to obtain a given density ρ_1 of the heavier liquid:

$$m_s = \frac{\rho_1 - \rho_2}{\rho_s - \rho_2}\rho_s V \tag{31}$$

V is the total volume occupied by the heavier liquid and ρ_s is the density of the salt (NaCl).

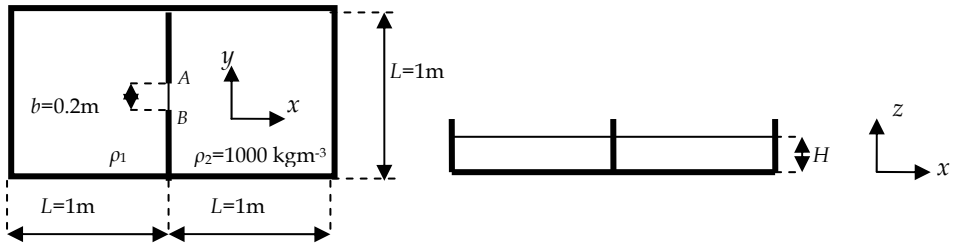

Fig. 5. Setup of the 3D lock exchange release experiment

The solution of water and salt is then coloured, in order to make easier the image analysis, and its actual density is measured by means of a picnometer. The runs considered are resumed in table 1.

6. Results

6.1 Validation of the mathematical models and the numerical methods

The mathematical models proposed in this chapter have to be validated reproducing results concerning with 2D gravity currents, because in literature there is a very wide choice of such results. Reference is made to 2D gravity currents generated by the full depth lock exchange release experiment. This latter is performed in a long and narrow channel (ratio width b over length L: $b/L<<1$) so the prevailing longitudinal dimension L makes possible a reliable representation of the gravity current on the xz plane. In such a channel the lock is situated at a distance x_0 from the wall. If the initial height of the heavier and the lighter liquid is the same, the lock exchange release is classified as full depth, otherwise as fractional depth. In this latter case, the ratio φ of the initial height of the heavier liquid h on the total height H is an important parameter of the experiment, known as fractional depth.
The evolution of a 2D gravity current originated by a lock exchange release experiment is characterised by four phases: the very initial phase, the slumping phase, the self-similar or

inertial phase and the viscous phase. As soon as the lock is removed and after the very initial phase, the heavier liquid starts travelling forward, while the lighter liquid starts travelling backward. The slumping phase is characterised by a constant advancing velocity U_f and a constant height h_f of the heavier front and it ends as soon as the bore, caused by the reflection of the lighter front with the wall, reaches the gravity current's front (Ungarish & Zemach, 2005). In lock of finite length x_0 the reflected wave reaches the forward advancing heavier front at a given instant of time, after which, the self-similar phase, characterised by time decreasing height and front velocity, starts. The viscous forces assume gradually increasing importance with respect to the inertial forces and eventually prevail on them. During the viscous phase the velocity of the front decreases more rapidly with time, with respect to the self-similar phase. Quite a long distance is required by the 2D gravity currents in order to develop the viscous phase (Huppert, 1982) and the evolution of experimental gravity currents is generally limited to the first three phases, i.e. until the self-similar phase.

Run	ρ_1 [kgm^{-3}]	H [cm]	V [m^3]	m_s [kg]	ε [mm]
1	1025	15	0.15	6.98	0.0
2	1015	15	0.15	4.19	0.0
3	1055	15	0.15	15.36	0.0
4	1015	15	0.15	4.19	0.7
5	1015	15	0.15	4.19	1.0
6	1015	15	0.15	4.19	1.6
7	1015	15	0.15	4.19	3.0
8	1025	15	0.15	6.98	0.7
9	1025	15	0.15	6.98	1.0
10	1025	15	0.15	6.98	1.6
11	1025	15	0.15	6.98	3.0
12	1017	10	0.10	3.17	3.0
13	1018	20	0.20	6.70	3.0
14	1028	10	0.10	5.21	3.0
15	1033	20	0.20	12.29	3.0
16	1019	15	0.15	5.31	3.0
17	1030	15	0.15	8.38	3.0
18	1017	10	0.10	3.17	0.0
19	1018	15	0.15	5.03	0.0
20	1019	20	0.20	7.08	0.0
21	1033	10	0.10	6.14	0.0
22	1033	15	0.15	9.22	0.0
23	1033	20	0.20	12.29	0.0

Table 1. Experimental runs

The behaviour of 2D gravity currents will be reproduced integrating numerically the "simplified" mathematical model, consisting of the one-layer partial differential system (29), the partial differential system for the correction term (30) and the Poisson equation (13), with the RHS calculated in correspondence of the one-layer solution $\mathbf{U_0}$. This "simplified" mathematical model will be hereinafter denoted as the 3D partial differential system.

Moreover, setting the y velocity components to zero (V_i=0; i=1,2) in the constant density equations (11) and omitting the derivatives with respect to y, it can be shown (Rottmann & Simpson, 1983; Ungarish & Zemach, 2005) that the pressure P_s can be eliminated from the motion equations and that the original five partial differential equations system (11) can be reduced to a partial differential system of two equations, hereinafter indicated as RL2D. This latter will be solved, by means of a Lax-Wendroff method, to obtain 2D numerical results. It is worth mentioning that all of numerical integrations were performed adopting the boundary conditions imposed on the velocities at the rigid walls of the tank. In literature (Ungarish, 2009b), a boundary condition imposed on the gravity current's front is usually adopted for 2D numerical gravity currents, except rare examples (D'Alessio et al., 1996). The choice of avoiding to impose a boundary condition on the gravity current's front is motivated by the fact that for 3D gravity currents it is very difficult or perhaps not possible to adopt a front condition. The validation process is also aimed to check the reliability of such a choice.

The slumping phase of gravity currents can be highlighted by experiments where the length of the lock is half of the total length of the channel (Shin et al., 2004; Lowe et al., 2005). In this case the velocity of the gravity current's front is quite well predicted by the Benjamin's formula for energy-conserving gravity currents (Shin et al., 2004). The experimental gravity currents considered in Lowe et al. (2005), with ratio r ($r=\rho_2/\rho_1$) in the range $0.607<r<0.993$, were realized in a channel, covered with a rigid lid, length L ($L\approx$2 m), wide b (b=0.23 m) and filled up to the height H (H=0.2 m). In Fig. 6a, b the time history of the non dimensional position of the gravity current's front is plotted versus non dimensional time. The scaling is defined by: $t^* = t\sqrt{g' h_0}\,/h_0$, $x^* = x/h_0$.

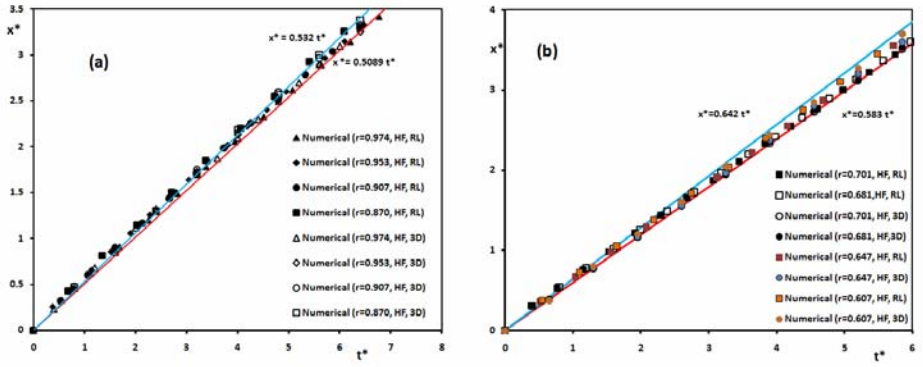

Fig. 6. a,b Slumping phase of Boussinesq (r>0.8) and non-Boussinesq (r<0.8) gravity currents

The results plotted in Fig. 6a,b are in good agreement. An interesting information can be obtained considering how the numerical data approximate the analytical value of the front velocity predicted by the energy conserving theory of Benjamin (Shin et al., 2004). This analytical value is equal, in dimensionless terms, to: $u_f = \sqrt{1/2r}$. The angular coefficients of the red and blue straight lines plotted in Fig. 6a,b, reported on the plot, are the non dimensional values of the analytical front velocity, obtained with the least (blue line) and the largest (red line) value of the ratio r. The agreement is quite good, showing that the 3D

partial differential system is able to reproduce 2D numerical results, when integrated in a 2D geometry, for quite a wide range of the density ratio.

The numerical and experimental space-time evolution of the thickness of the gravity current is shown in Fig. 7. Numerical results are obtained solving the RL2D partial differential system, the 3D partial differential system and the 2L2D partial differential system, obtained setting to zero the pressure P_s, the y velocity components and eliminating the derivatives with respect to y in the partial differential system (9). This 2L2D partial differential system, consisting of four partial differential equations, is able to describe the evolution of the gravity current thickness h_1 and the upper surface h_1+h_2. The experimental results shown in Fig. 7 were obtained by means of a full depth lock exchange release experiment, conducted at the hydraulic lab of the DEHMA of the Politechnical University of Catalunya, in a transparent channel (length L=2 m, width b=0.2 m, height H=0.35 m), with salty (ρ_1=1100 kgm^{-3}) and fresh water (ρ_2=1000 kgm^{-3}). The initial height of the lock was h_1=0.28 m. The profiles are relative to 1 and 3 sec after the removal of the lock. The agreement between the experimental and the 2L2D numerical profiles is good. From Fig. 7, it is evident that the mathematical model is able to describe the evolution of the gravity current, which is in its slumping phase. The 2L2D numerical profile of the gravity current is in good agreement with the experimental profile not only concerning with the position of the front, but also with the position of the forward advancing bore, which gradually approaches the front.

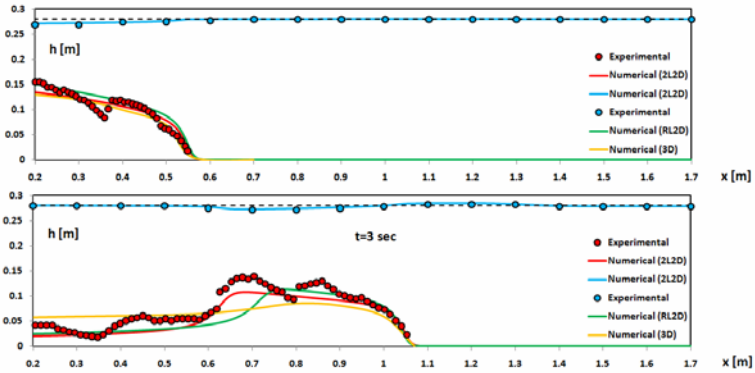

Fig. 7. Numerical and experimental profiles of a 2D gravity current

It is also surprising to see how the form of the gravity current is quite well reproduced by the 2L2D numerical results, despite of the fact that the entrainment of lighter liquid is neglected. The upper surface profile is well reproduced too. It is interesting to observe that the amplitude of the motion of the upper surface is small with respect to the gravity current's thickness. This fact justifies the rigid-lid hypothesis, whose validity depends on the value of the density ratio r: the smaller this ratio, the larger the amplitude of the free surface motion and the less reliable is the rigid-lid hypothesis (D'Alessio et al., 1996). The agreement between the experimental and the RL2D numerical profiles is fairly good. Indeed, it is evident from Fig. 7 that the RL2D simulations slightly overestimate the velocity of the forward advancing bore, with respect to the 2L2D numerical results, and then underestimate the position x_s where the bore reaches the front. This underestimation of x_s is typical for the RL2D simulations and it is also confirmed in the work of Ungarish and

Zemach (2005). At last, it is interesting to observe that the ratio of the height of the gravity current, just behind the front, on the initial height, is approximately equal to 1/3. This fact is in agreement with the theory of Benjamin (Shin et al., 2004), which predicts a value for such a ratio equal to 0.347 for the most dissipative gravity current. The experiments generally confirm that this kind of gravity current occurs during the slumping phase, after the bore is reflected from the left wall of the channel. The agreement between the experimental and the 3D numerical profiles is fairly good too.
The 2L2D and RL2D numerical simulations were obtained on a grid with approximately 10^3 computational points and a time step with an order of magnitude of 10^{-4} sec. The 3D numerical simulations were obtained on a grid with approximately 10^5 spatial cells and a time step with an order of magnitude of 10^{-5} sec.

6.2 Experimental and numerical results on 3D gravity currents

All of the experiments listed in Table 1 have been numerically reproduced, but for obvious reasons of space not all of the results will be presented.
In Fig. 8, the comparison between the experimental and numerical time histories of the position and the velocity of the front along x direction are shown. With reference to Table 1, curves plotted in Fig. 8 are relative to runs 1,2,4,5,6,8,9,10. Non dimensional time t^*, position x^* and velocity u^* are scaled as: $t^* = \frac{t}{h_0/\sqrt{g' h_0}}$, $x^* = \frac{x}{L}$, $u^* = \frac{u}{\sqrt{g' h_0}}$. The position of the numerical front has been determined as in La Rocca et al. (2008). The agreement between the experimental and numerical results is fairly good for all of the cases. Indeed, the error, defined as in La Rocca et al. (2008), is no larger than 11%, which is a reasonable and consistent value with regard to the limits of the mathematical model and the experimental uncertainties. Numerical results plotted in Fig. 8 have been obtained by solving the one-layer partial differential system (29), i.e. without considering the correction due to the pressure P_s. This fact shows as the one-layer model is able to reproduce the dynamics of the 3D gravity current, while the correction gives information on the upper layer dynamics.
Both the experimental and numerical curves plotted in Fig. 8 show a two-phase dynamics during the evolution of the gravity current: an accelerating phase followed by a decelerating phase. The first phase is dominated by inertial-buoyancy forces, while during the second phase the effects of the friction force gradually become evident, through a reduction of the front's velocity. The fact that the reduction of the front velocity occurs during the second phase of motion is in qualitative agreement with the results of other works on 2D gravity currents flowing on a rough bottom (Hogg & Woods, 2001).
Discrepancies between numerical and experimental data occur mainly during the first phase of motion, i.e. the accelerating phase, and are due to a general overestimation of the numerical front velocity during this phase. This overestimation of the front velocity could be caused both by the difference between numerical and experimental initial conditions and by the intrinsic limitation of the mathematical model. The difference between numerical and experimental initial conditions is concerned with the removal of the lock: it is instantaneous in the numerical code, while it occurs during a finite interval of time in the laboratory experiments. Such a difference affects the motion of the gravity current during the first instants of motion. With regard to the intrinsic limitations of the mathematical model, it is worth mentioning that (Klemp et al., 1994) the shallow water and the one-layer approximations are questionable during the very initial phase of motion.

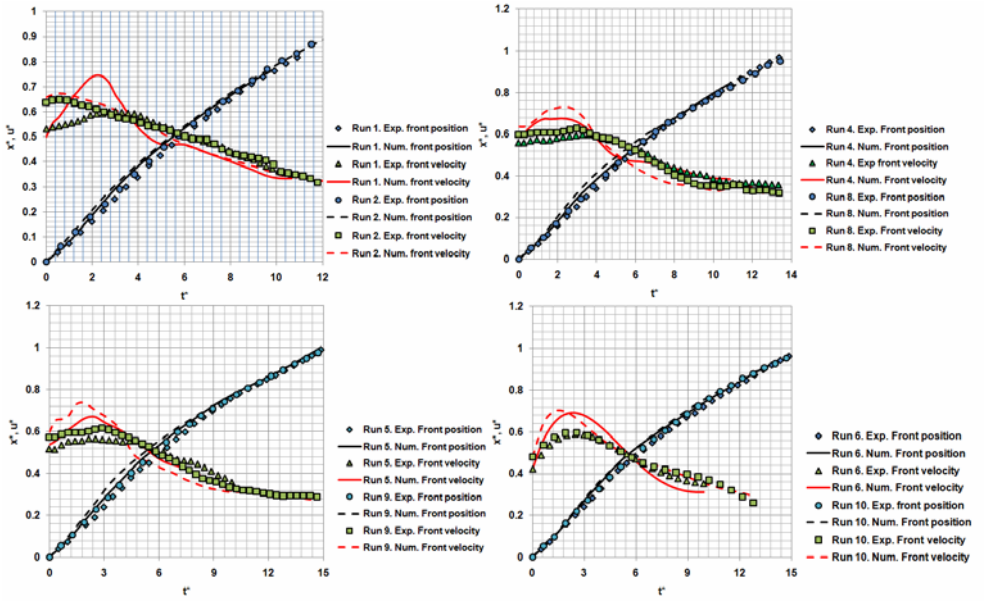

Fig. 8. 3D gravity current. Non dimensional front position x^* and velocity u^* versus non dimensional time t^*. Runs 1,2,4,5,6,8,9,10

In Fig. 9 the numerical and experimental top views of the gravity currents corresponding to the runs 2,4,5 at different instant of times are shown. These top views give an idea of the ability of the mathematical model and of the numerical method in reproducing the evolution of the gravity current not only along the x direction. The agreement between numerical and experimental results is quite good, except for the region near the gate, which is the most critical region of the flow, due to the high gradients of the hydrodynamic quantities in correspondence of the edges of the gate.

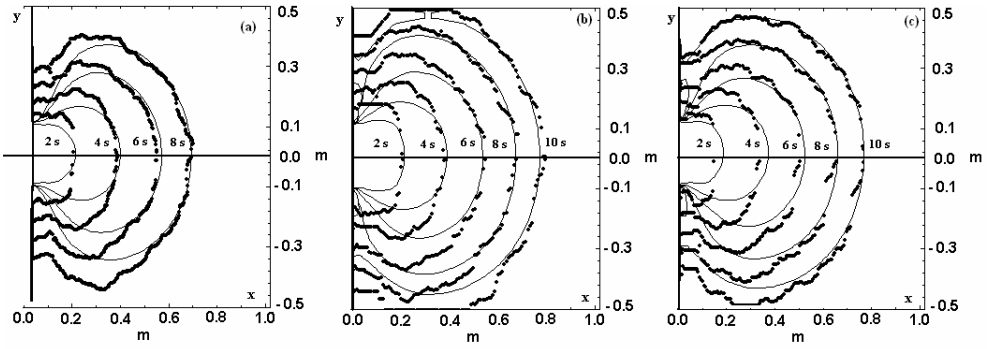

Fig. 9. Numerical and experimental top views of the gravity currents at different instants of time

The solution of the 3D partial differential system determines the motion of the upper layer. Presently no experimental results are at disposal to verify the correctness of the numerical

results. Nevertheless the numerical pressure and velocity fields are consistent with the experimental observations. Those plotted in Fig. 10a,b refer to the run 9, 5.6 sec after the removal of the gate. The structure of the velocity field of the gravity current and the lighter layer is shown in Fig.10a. Thanks to the symmetry of the flow field, Fig. 10a reproduces only half of the fluid domain. The top velocity field refers to the gravity current, while the bottom velocity field refers to the lighter liquid. The choking effect caused on the flow by the narrow opening of the gate is highlighted by the high values of the velocity attained in correspondence of the opening, which is the most critical region of the flow, due to the high value attained by the radius of curvature of the streamlines at the edges of the gate.

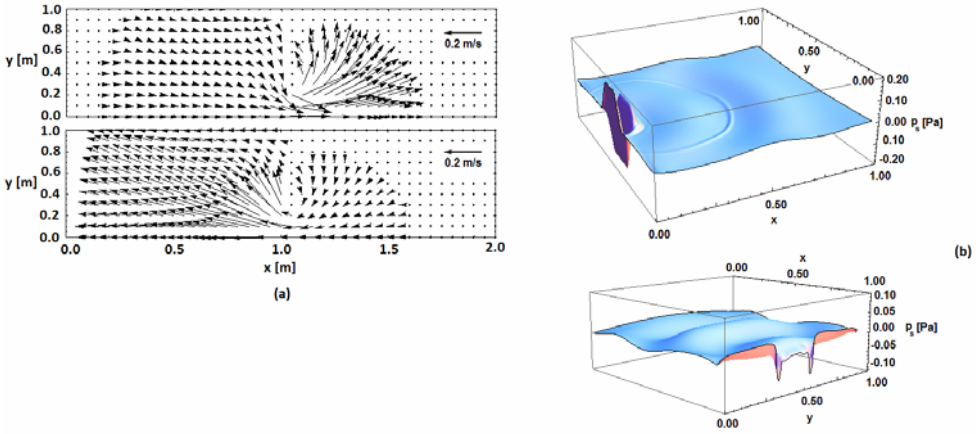

Fig. 10. a,b Velocity and pressure fields. Run 9, 5.6 seconds after the removal of the gate

The pressure field shown in Fig.10b shows that, apart from the region of the gate, the pressure P_s vanishes. This fact justifies the use of the one-layer model for modelling the dynamics of the 3D gravity currents. The plot is divided, for the sake of clarity of representation, into two parts, corresponding to the left and right parts of the tank shown in Fig. 5. In the region of the gate the pressure P_s shows large variations in small spatial intervals, corresponding to the strong deformation of the gravity current and to the sudden increase of velocity of this latter across the gate.

Another interesting feature reproduced by the pressure field, is the line of the gravity current's front, which is clearly apparent on the plot reproducing the right side of the tank (Fig. 10b). This pressure front corresponds to the gravity current's front velocity, shown in Fig. 10a, and separates the advancing front of heavier liquid from the quiescent lighter liquid.

Looking at the velocity field shown in Fig. 10a, it is possible to observe that along the streamline y=0 (the symmetry streamline) the y velocity components V_1, V_2 vanish. Consequently, equation (14) becomes:

$$\frac{\partial(U_1 h_1 + U_2 h_2)}{\partial x} = 0 \quad \Rightarrow \quad U_1 h_1 + U_2 h_2 = const \tag{39}$$

The constant is set to zero, due to the fact that on the wall U_1=U_2=0. As a consequence of (39), the velocity of the lighter layer U_2 along the streamline is related to that of the heavier layer U_1 by the algebraic relation:

$$U_2 = -U_1 \frac{h_1}{H - h_1} \tag{40}$$

The simple relation (40) permits an interesting check on the validity of the numerical results, shown in Fig. 11.

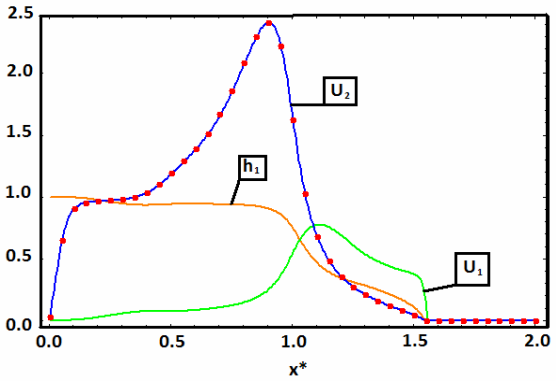

Fig. 11. Dimensionless profiles of the gravity current's thickness and the velocities. Run 9, 5.6 sec after the removal of the lock

In Fig.11 the dimensionless profile of the gravity current's thickness h_1/H (the orange line) and the dimensionless profile of the velocities $\frac{U_1}{\sqrt{g'H}}, \frac{U_2}{\sqrt{g'H}}$ (respectively the green and the blue line) along the simmetry streamline are plotted. The data refer to the run 9, 5.6 sec after the removal of the lock. The dotted line represents the velocity of the upper layer, calculated according to (40). The agreement between the dotted line and the continuous blue line is very good, showing that numerical data are consistent with the mathematical model. It is also worth noting the agreement on the position of the front, between the profile of the gravity current and the velocity profile U_1.

The numerical results considered until now were obtained assuming constant the densities of the two liquid layers. Nevertheless, in many circumstances of environmental importance, this assumption does not make sense. It is the case of the turbidity currents, which occur under a deep layer of fresh water (in lakes or seas) and consists of a mixture of water and heavy sediment. The most important feature in turbidity current's dynamics is that the sediment settles down and possibly can be put in re-suspension during the evolution of the current, then varying the concentration C and consequently reducing the excess density (17) and the driving buoyancy force (Hogg et al., 2000). In order to have an idea of the effect of settling of sediment on the turbidity current's dynamics, a numerical experiment inspired by the experimental work of Bonnecaze et al. (1993) has been performed. Bonnecaze et al. (1993) compared the behavior of 2D turbidity currents with the behavior of a 2D gravity current, all of them having the same initial excess density. The turbidity currents were realized making a suspension of water and silicon carbide particles with increasing diameter (9μm≤d_s≤53μm). The numerical experiment presented here refers to the comparison between the numerical results of run 2 (ρ_1=1015 kgm^{-3}) and the numerical results relative to turbidity currents with the same initial density, but realized with a mixture of water and silicon carbide particles, with increasing diameter (9μm≤d_s≤53μm). Numerical results were

obtained solving the equations (18), (19) and are shown in Fig. 12a,b. In Fig. 12a the numerical time histories of the current's front position are plotted.

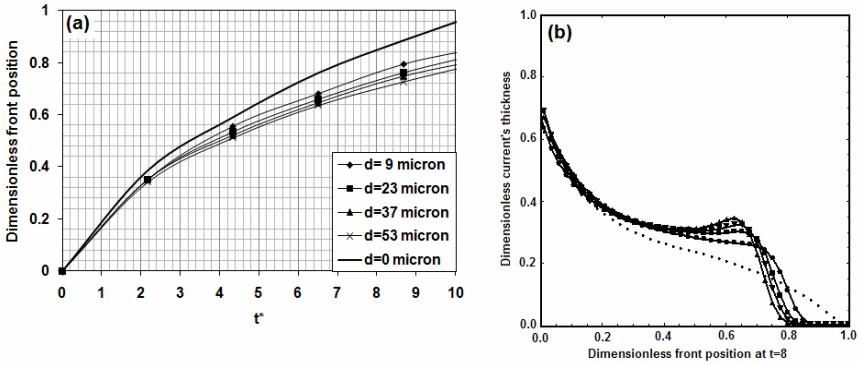

Fig. 12. Comparison between the constant density gravity current and the turbidity currents obtained with particles of increasing diameters

The front position is dimensionless and the scaling factor is represented by the front position attained by the gravity current 10 s after the start of the run. So the values on the vertical axis represent the percentage of the distance travelled at any instant of time by the turbidity current's front, with respect to that travelled by the gravity current's front. The time is scaled as: $t^* = \dfrac{t}{h_0/\sqrt{g' h_0}}$. The general behavior is in qualitative agreement with that shown in Bonnecaze et al. (1993): as the diameter of the sediment increases, the front velocity decreases. Indeed, the settling of larger particles occurs more rapidly, thus making more effective the reduction of the excess density and then of the driving buoyancy force. The influence of the particles settling on the profile of the current's thickness is shown in Fig. 12b. In this figure, the thickness profiles, obtained at t*=8 and relative to the currents considered in Fig. 12a, are shown. The dotted line represents the gravity current; the circles, the squares, the overturned triangles and the upright triangles represent the turbidity currents made with diameters d_S respectively of 9 μm, 23 μm, 37 μm and 53 μm. The profiles are scaled with the initial height (H=0.15 m), while the abscissa is scaled with the distance travelled by the gravity current at t*=8.

Settling of particles causes a distortion of the gravity current profile. The distortion increases with the diameter of the particle. Nevertheless the volume of the gravity current remains practically constant. Indeed, the relative variation of volume is equal to 1.35% in the case of the turbidity current showing the maximum distortion, realized with particles of diameter d_S=53 μm.

6.3 Numerical simulation of entrainment at Flix reservoir

A qualitative study of the contamination event occurred in the Flix reservoir has been carried out by means of the software BANG 1DT (Herrero et al., 2009), firstly with a simple bathymetry consisting in a variable slope that ends in a horizontal section, secondly considering the actual bathymetry of the reservoir. BANG 1DT is essentially based on the one dimensional version of the equations (18), (19) and (26). The study was focused on the

influence of the slope, the initial velocity, the initial concentration of sediment and the temperature of water on the evolution of the density current, which could have caused the contamination of the Flix reservoir. In Figure 13 are plotted the profiles of the depth of the density current, of its velocity and density, at different instants of time, versus the distance travelled by the density current. These profiles have been obtained by BANG 1DT starting from the following initial conditions:

- slope: 1.0 %
- initial velocity: 1.0 m/s
- initial concentration: 0.05 mg/kg
- initial temperature: 7.0 ºC
- external temperature: 15.0 ºC
- sediment temperature: 15.0 ºC

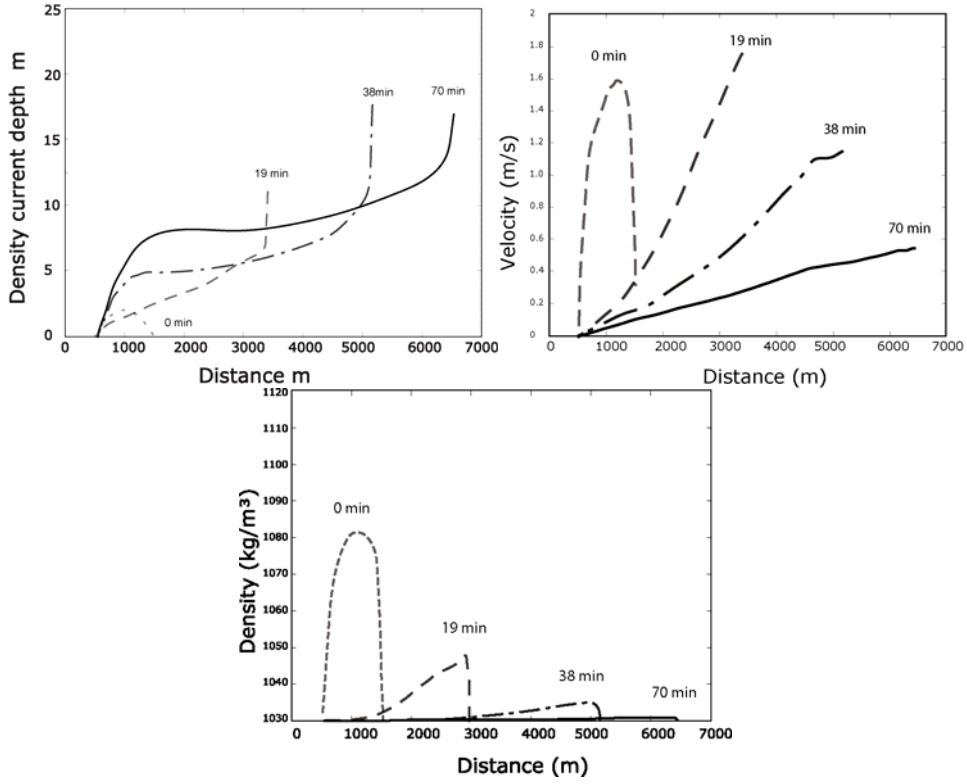

Fig. 13. Depth, velocity and density distribution of the density current along its path

The analysis of the case shown in Figure 13, as well as that of other cases (not reported here), showed that:

a. the difference of temperature between two water bodies has a slight influence on the evolution of the density current, although this latter can be also caused by such a difference. The evolution of the density current is dominated by the gradients of sediment concentration.

b. Sedimentation and erosion depend on the velocity of the density current.
c. The qualitative behaviour of the density current is not affected by the slope of the bottom, while the erosion increases with the slope.

The influence of the initial length of the density current on the scour profile is also an interesting issue. Initial lengths of 500, 1000 and 1500 meters have been considered (Figure 14).

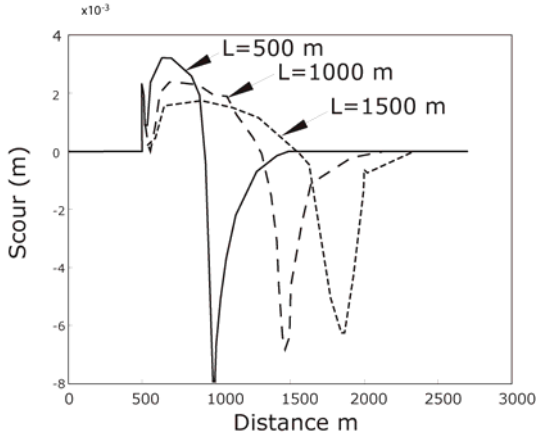

Fig. 14. Scour profile produced during the passage of the density current for three different initial lengths 500 m, 1000 m and 1500m

As the current length increases, the maximum depth of the scour decreases but the total volume of entrained sediment increases. This latter quantity is of primary importance and once it has been obtained, it is possible to compute the quantity of contaminant set into movement, starting from the concentration of this element at the bottom of the reservoir, obtained by means of suitable measurements procedures.

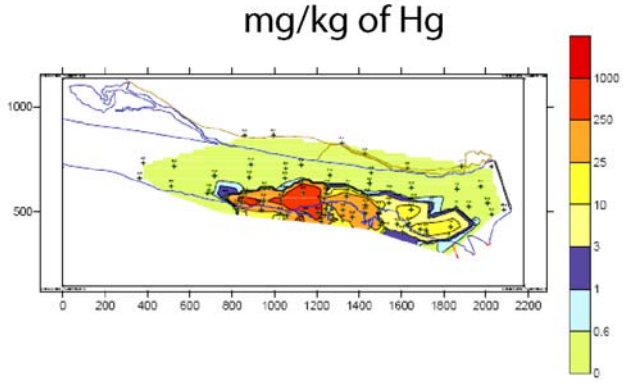

Fig. 15. Distribution of the concentration of Hg in the sediment fan in front of the chemical enterprise (Herrero et al. 2009)

As an example, in Figure 15 is shown the concentration of Hg at the bottom of the Flix reservoir after the contamination event (Herrero et al. 2009). In Table 2 are given the entrained volumes of sediment corresponding to the initial velocity of 1.0 m/s and 3.0 m/s and calculated by means of the scour profiles determined by BANG 1DT. Considering a density current 30 meters wide (a reasonable value for the considered case), these results would imply the mobilized volumes of mercury shown in the same Table. Assuming that the sediment entrained by the current has an average mercury concentration of 200 mg/kg and taking the value of 2650 kg/m^3 as characteristic for the density of sediment, the amount of mobilized mercury shown in Table 2 are obtained.

Initial velocity (m/s)	Eroded volume per width unit (m^3/m)	Mobilized volume (m^3)	Mass of mercury mobilized (kg)
1.0	1.5	45	23.85
3.0	18	540	286.2

Table 2. Eroded volume per unit width due to two different initial velocities current

These values have the same order of magnitude of those measured in water samples. The results obtained by the numerical model then give only a qualitative indication, which however confirms the potential dangerousness of the density current, as a cause for the mobilization of contaminated sediment in water bodies, and explains the contamination event of Flix as due to the formation of a density current. In this case study, the complexity of the geometry is one of the sources of uncertainty. The non-availability of the exact bathymetry of the upstream section of the river Ebro e.g. hindered a more realistic simulation of the density current and is then considered as a major weak point.

7. Conclusion

This chapter deals with mathematical, experimental and numerical modelling of 3D gravity currents. The motivation is that this kind of gravity currents has not been so frequently examined in scientific literature as 2D and axisymmetric gravity currents.

Two main cases have been examined: the constant density and the variable density case. Concerning with the constant density case, the attention has been focused on the problem of the double layer formulation and the determination of the pressure at the upper surface when the rigid lid hypothesis is assumed. A suitable simplified procedure has been proposed for solving the equations of motion and the Poisson's equation for the pressure. Concerning with the variable density case, the attention has been focused on the extension of known 2D mathematical models and on the effect of the resuspension and sedimentation dynamics in 3D turbidity current.

The comparison between numerical and experimental results, which refer to the simulation of 3D gravity currents, shows that the constant density, two-layer mathematical model reproduces correctly the key features of the dynamics of the considered physical phenomenon. Numerical results obtained in the variable density case make sense and are in qualitative agreement with the experimental observations found in literature.

Future work should go along two main directions: a systematic validation of the constant density, two-layer mathematical model and the realisation of an exhausting experimental campaign on 3D turbidity current.

At last a case study, concerning with the contamination event of the Flix reservoir has been considered. Results have to be carefully managed, due to the complexity of the phenomenon and to its intrinsic uncertainties. Nevertheless it is possible to claim that density and turbidity currents can be responsible for contamination of water bodies, as in this case study. This fact is a strong motivation for further studies on this subject.

8. References

Benjamin, T. B. (1968). Gravity currents and related phenomena. *J Fluid Mech*, Vol. 31, n. 2, 209-248

Bonnecaze, R. T.; Huppert, H. E.; Lister, J. (1993). Particle-driven gravity currents. *J Fluid Mech*, Vol. 250, 339

Birman, V. K.; Martin J. E.; Meiburg E. (2005) The non-Boussinesq lock-exchange problem. Part 2. High-resolution simulations. *J Fluid Mech*, Vol. 537, 125-144

Birman, V. K.; Meiburg E.; Kneller, B. (2009) The shape of submarine levees: exponential or power law? *J Fluid Mech*, Vol. 619, 367-376

Bradford, F. S.; Katopodes, N. D.; Parker, G. (1997). Characteristic analysis of turbid underflows. *Journal of Hydraulic Engineering*, Vol. 123, no. 5, 420-432

Cantero, M. I.; Balachandar, S.; Garcia, M. H. (2008) An Eulerian-Eulerian model for gravity currents driven by inertial particles, *International Journal of Multiphase Flow*, Vol. 34, 484-501

Çengel, Y. A. & Cimbala, J. M. (2006) *Fluid Mechanics: Fundamentals and Applications*. Mc Graw-Hill, New York

Costa, J.; Villarubia, M.; Bateman, A. 2004. Contribución y Evaluación del " Estudi de la Dinámica dels Compostos Otganoclorats Persistents i Altres Contaminants en els Sistemes Aquàtics Continentals" Noviembre 2003. Propuesta de Actuaciones en el Embalse de Flix. Universidad Politécnica de Cataluña-Universidad de Barcelona.

D'Alessio, S. J. D.; Moodie, T. B.; Pascal, J. P.; Swaters, G. E. (1996). Gravity currents produced by sudden release of a fixed volume of heavy fluid. *Studies in Applied Mathematics*, Vol. 96, 359-385

Dietrich, E. W. (1982). Settling velocity of natural particles. *Water Resour. Res*. Vol. 18, 1626

Fischer, H.B.; List, J. E.; Koh, R. C. Y.; Imberger, J.; Brooks, N. H. (1979). *Mixing in inland and coastal waters*. Academic Press

Garabedian, P. R. (1964). *Partial differential equations*. J. Wiley and Sons, New York

García, M. H. & Parker, G (1993). Experiments on the Entrainment of Sediment into Suspension by a Dense Bottom Current. *AGU Journal of Geophysical Research (Oceans)*, Vol. 98, no. C3 (March), 4793-4807.

Hallworth, M.; Huppert, H. E.; Ungarish, M. (2001). Axisymmetric gravity currents in a rotating system: experimental and numerical investigations. *J Fluid Mech*, Vol. 447, 1-29

Hallworth, M.; Huppert, H. E.; Ungarish, M. (2003). On inwardly propagating high-Reynolds-number axisymmetric gravity currents. *J Fluid Mech*, Vol. 494, 255-274

Härtel, C.; Meiburg, E., Necker, F. (2000a) Analysis and direct numerical simulation of the flow at a gravity-current head. Part 1. Flow topology and front speed for slip and no-slip boundaries. *J. Fluid Mech.*, Vol. 418, 189-212

Härtel, C.; Carlsson, F., Thunblom, M. (2000b) Analysis and direct numerical simulation of the flow at a gravity-current head. Part 2. The lobe-and-cleft instability. *J. Fluid Mech.*, Vol. 418, 213-229

Herrero, A.; Medina, V.; Bateman, A. (2009) Evaluation of resuspension due to density currents in Flix reservoir (Spain). *Proceedings of River Coastal and Estuarine Morphodynamics*, Santa Fé Argentina

Hogg, A.J.; Ungarish, M.; Huppert, H.E. (2000) Particle-driven gravity currents: asymptotic solutions and box models. *European Journal of Mechanics B. Fluids* Vol. 19, 139-165

Hogg, A. J. & Woods, A. W. (2001) The transition from inertia-to-bottom-drag-dominated motion of turbulent gravity current. *J. Fluid Mech.*, Vol. 449, 201-224

Huang, H.; Imran, J.; Pirmez, C. (2005) Numerical Model of Turbidity Currents with a Deforming Bottom Boundary. *Journal of Hydraulics Research*, Vol. 131, no. 4, 283-293

Huppert, H.E. (1982) The propagation of two-dimensional and axisymmetric viscous gravity currents over a rigid horizontal surface. *J. Fluid Mech.*, Vol. 121, 43–58

Huppert, H. E. (2006) Gravity currents: a personal perspective. *J Fluid Mech*, Vol. 554, 299-322

Huppert, H. E. & Simpson, J. E. 1980 The slumping of gravity currents. *J. Fluid Mech.,* Vol. 99, 785–799.

Karman, T. Von (1940). The engineer grapples with nonlinear problems. *Bull. Am. Math. Soc.*, Vol. 46, 615.

Keulegan, G. H. (1957). An experimental study of the motion of saline water from locks into fresh water channels. *Nat. Bur. Stand. Rept.* 5168

Klemp, J. B.; Rotunno, R.; Skamarock, W. (1994) On the dynamics of gravity current in a channel. *J Fluid Mech*, Vol. 269, 169-198

Kostic, S.; Parker, G. (2007) Conditions under which a supercritical turbidity current traverses an abrupt transition to vanishing bed slope without a hydraulic jump. *J. Fluid Mech.*, Vol. 586, 119-145

La Rocca, M.; Adduce, C., Sciortino, G., Bateman Pinzon, A. (2008) Experimental and numerical simulation of three-dimensional gravity currents on smooth and rough bottom. *Physics of Fluids*, Vol. 20,1-15

La Rocca, M.; Adduce, C.; Mele, P.; Sciortino, G. (2009) Numerical simulation of 3D submarine turbidity currents. *Proceedings of ISOPE 2009*, pp. 1-8, Osaka, June 2009

La Rocca, M.; Bateman Pinzon, A. (2010) A perturbative method for double-layer shallow water equations. *Proceedings of CIMW 2010*, pp. 1-8, ISBN, Barcelona, June 2010

Launder, B. E. & Spalding, D. B. (1972) *Mathematical Models of Turbulence*. Academic Press, London

Lowe, R. J.; Rottman, J. W.; Linden, P. F. (2005) The non-Boussinesq lock-exchange problem. Part 1. Theory and experiments. *J Fluid Mech*, Vol. 537, 101-124

Lee, W. H.; Lyczkowski, R. W. (2000). The basic character of five two-phase flow model equation sets. *International Journal for Numerical Methods in Fluids*, Vol. 33, 1075-1098

Lyczkowski, R. W.; Gidaspow, D.; Solbrig, C. W.; Hughes, E. D. (1978). Characteristics and stability analysis of transients one-dimensional two-phase flow equations and their finite difference approximations. *Nucl. Sci. Eng.*, Vol. 66, 378-396

Patterson, M. D.; Simpson, J. E.; Dalziel, S. B.; Van Heijst, G. J. F. (2006) Vortical motion in the head of an axisymmetric gravity current. *Physics of fluids*, Vol. 18, 1-7

Parker, G.; Fukushima, Y.; Pantin, H. M. (1986) Self-accelerating turbidity currents. *J. Fluid Mech*. Vol. 171, 145–181.

Pedloski, J. (1987). *Geophysical Fluid Dynamics*. Springer Verlag, Berlin/New York

Prandtl, L. (1952) *Essentials of Fluid Dynamics*. Haffner, New York

Pratson, L.; Imran, J.; Hutton, E.; Parker, G.; Syvitski, J. P. G. (2001). Bang 1-D: a one-dimensional Lagrangian model of turbidity currents mechanics. *Computers and Geosciences*, Vol. 26, no. 7, 705–720

Ross, A. N.; Linden, P. F.; Dalziel, S. B. (2002). A study of three dimensional gravity current on a uniform slope. *J Fluid Mech*, Vol. 453, 239-261

Rottman, J. W.; Simpson, J. E. (1983) Gravity currents produced by instantaneous releases of a heavy fluid in a rectangular channel. *J Fluid Mech*, Vol. 135, 95-110

Shin, J. O.; Dalziel, S. B.; Linden, P. F. (2004) Gravity currents produced by lock exchange. *J Fluid Mech*, Vol. 521, 1-34

Simpson, J. E. (1997). *Gravity Currents in the Environment and the Laboratory*. Cambridge University Press, Cambridge

Simpson, J. E. & Britter, R. E. (1979). The dynamics of the head of a gravity current advancing over a horizontal surface. *J. Fluid Mech.*, Vol. 94, 477–495.

Stoker, J. J. (1957). *Water waves*. Interscience Publishers Inc., New York

Toro, E. F. (1999) *Riemann Solvers and Numerical Methods for Fluids Dynamics*. Springer, New York

Ungarish, M. (2007a). A shallow-water model for high Reynolds number gravity currents for a wide range of density differences and fractional depths. *J Fluid Mech*, Vol. 579, 373-382

Ungarish, M. (2007b). Axisymmetric gravity currents at high Reynolds number: On the quality of shallow-water modeling of experimental observations. *Physics of fluids*, Vol. 19, 1

Ungarish, M. (2008). Energy balances and front speed conditions of two-layer models for gravity currents produced by lock release. *Acta Mech*, Vol. 201, 63-81

Ungarish, M. (2009). Energy balances for gravity currents with a jump at the interface produced by lock release. *Acta Mech*, Vol. 211

Ungarish, M. (2009b). *An introduction to gravity Currents and intrusions*. Chapman & Hall/CRC press, Boca Raton, London, New York

Ungarish, M. (2010) The propagation of high-Reynolds-number non-Boussinesq gravity currents in axisymmetric geometry. *J Fluid Mech*, Vol. 643, 267

Ungarish, M.; Zemach, T. (2005) On the slumping of high Reynolds number gravity currents in two-dimensional and axisymmetric configurations. *European Journal of Mechanics B/Fluids*, Vol. 24, 71-90

Yih, C. S. (1947) *A study of the characteristics of gravity waves at a liquid interface*. M.S. Thesis, State Univ. of Iowa